Plasmonic Nano-antenna Optimization Using Characteristic Mode Analysis

Sumitra Dey, *Student Member, IEEE*, Deb Chatterjee, *Senior Member, IEEE*, Edward J. Garboczi, and Ahmed M. Hassan, *Senior Member, IEEE*

***Abstract*— Plasmonic nano-antennas are typically designed with RF-inspired rigorous parametric optimization processes that lack proper physical insights. In this study, we demonstrate a systematic optimization approach for nano-antennas based on characteristic mode analysis (CMA). A complex geometry, designated as split-ring two-wire antenna (SRA), is selected and optimized using the CMA technique. CMA identifies the dominant modes of the structure at the frequency of interest as well as explains the dependency of the modes on the structure's shape, size and material properties. These insights from CMA have been used in the present study to efficiently optimize SRA shape, size, and material which yield more than 700 % near-field intensity enhancement (NFIE) at the desired operating frequency. This proposed CMA based optimization method can be adapted easily for many other nano-antenna applications, facilitating the development of improved nano-structures.**

***Index Terms*—Plasmonic, Nano-structures / Nano-antennas, Characteristic Mode Analysis (CMA), Surface Integral Equation (SIE), Method of Moments (MOM), Split-ring Two-wire Antenna (SRA), Near Field Intensity Enhancement (NFIE).**

I. INTRODUCTION

Engineered plasmonic nano-structures are currently being deployed extensively in a wide range of fields such as solar energy harvesting, non-linear optics, near-field scanning optical microscopy, photo-catalysis, metamaterials, quantum computing and many other sensing applications [1]-[2]. [1]This wide applicability comes from the outstanding characteristics of plasmonic materials such as extreme light trapping at the sub-wavelength vicinity of the nano-structure, manipulating and redirecting light well below the classical diffraction limits, enhancing the rate of photo-chemical reactions, and modulating thermal decay rates [2]-[3]. In this work, we will focus on enhancing the near-field intensity of a plasmonic nano-antenna. Generally, this enhancement is defined by the ratio of measured electric field intensity near the nano-antenna ($|E|^2$) to the illumination intensity in the absence of the nano-antenna ($|E_0|^2$), termed as the near-field intensity enhancement (NFIE), $|E|^2/|E_0|^2$ [2]. The magnitude of the NFIE can range from several hundred [4] to several thousand [5].

Extensive studies have been carried out to push the upper limit of the NFIE at a specified frequency by optimizing the shape and material of the nano-structure. The optimization process starts by defining a set of goals, known as fitness parameters. The shape of the nano-antenna is then varied computationally and iteratively until it meets the goal within a certain threshold. Most optimization techniques use the same general methodology, but they differ only in the specific evolutionary optimization algorithm (EA) and/or the electromagnetic (EM) solver used to calculate the electromagnetic response.

Examples of different EA/EM solver combinations previously reported include: the binary particle-swarm optimization (BPSO) algorithm combined with the Coupled Dipole Approximation (CDA) solver [6], the genetic optimization algorithm coupled with multi-particle Mie Theory [7], the repetitive perturbation technique combined with the Finite-Difference-Time-Domain (FDTD) solver [8], the Gielis' Super formula based stochastic optimization coupled with 2D boundary-element method solver [9], and the evolutionary search algorithm coupled with the FDTD solver [10]-[11]. The previously mentioned optimization techniques are basically iterative trial and error approaches, which lack proper physical insights and are computationally expensive.

In this present work, a different method for nano-antenna optimization is proposed where characteristic mode analysis (CMA) has been used to understand the physics of the near-field enhancement process, so that the nano-antenna shape, size, and material can be strategically optimized using lower computational time and memory requirements. CMA is basically an eigenvalue problem where the currents excited on the nano-antennas are decomposed into a weighted summation of fundamental modes [12]–[13]. At each frequency, the CMA

[1]Manuscript received XXXXXX; revised XXXXXX ; accepted XXXXXX . Date of publication XXXXXX ; date of current version XXXXXX. This work was supported in part by the NIST "Multi-Scale Computational Modeling of Carbon Nanostructure Composites" under Grant 70NANB15H285 and in part by NSF CRI Award 1629908 "II-NEW: Experimental Characterization and CAD Development Testbed for Nanoscale Integrated Circuits." (Corresponding author: Ahmed M. Hassan.) Partial contribution of the National Institute of Standards and Technology, not subject to US copyright.

S. Dey, D. Chatterjee and A. M. Hassan are with the Department of Computer Science and Electrical Engineering, University of Missouri–Kansas City, Kansas City, MO 64110 USA (e-mail: sumitra.dey@mail.umkc.edu; ChatD@umkc.edu; hassanam@umkc.edu).

E. J. Garboczi is with the Material Measurement Laboratory, Applied Chemicals and Materials Division, National Institute of Standards and Technology, Boulder, CO 80305 USA (e-mail: edward.garboczi@nist.gov).

Color versions of one or more of the figures in this paper are available online at http://ieeexplore.ieee.org.

This article has been accepted for publication in a future issue of this journal, but has not been fully edited. Content may change prior to final publication. Citation information: DOI 10.1109/TAP.2019.2938705, IEEE Transactions on Antennas and Propagation

provides the relative significance of each mode and defines how strongly it is coupled to the incident field. CMA has been extensively used for the analysis and design of RF and microwave antennas composed of perfect electric conductors (PEC) [14]-[16]. More recently, CMA was also employed for the design of antennas composed of lossless dielectrics and with simple canonical shapes [17]. However, in this work we focus on the CMA optimization of plasmonic nano-antennas, with complex shapes, composed of noble metals like gold and silver. In the infrared and visible frequency ranges, gold and silver behave more like lossy dielectrics than PEC leading to differences in the modal behavior that will be discussed in the following sections. Also, all of the previous CMA studies focused on optimizing the matching of the antenna feed or on optimizing its far-field radiation characteristics. However, this work shows for the first time the use of CMA for the optimization of a near-field property such as the near-field intensity enhancement (NFIE).

To the best of our knowledge, for nano scale designs, CMA has only been used for 1D structures, i.e. CNTs [18], or 2D structures like graphene [19], or canonical 3D shapes like spheres and rods [20]. In our present study, we have picked an arbitrary complex nano-antenna shape from the literature, called a split-ring-two-wire nano-antenna (SRA) hybrid [10], and improved its NFIE performance by more than 700 % at the desired operating frequency by using currently proposed CMA-based shape and material optimization technique. The process has been documented in detail in the following sections.

The organization of this paper is as follows: Section II discusses the geometry of SRA and analyzes its electromagnetic response using multiple electromagnetic solvers. Section III briefly reviews the CMA theory and explains how it can be adapted for the modal analysis of plasmonic nano-antennas. Section IV demonstrates the shape optimization process of SRA using dominant eigenmode information. Section V explains the correlation between plasmonic material properties and the eigenmode behavior and its impact on frequency specific performance optimization. Section VI documents the detailed development process of an improved SRA design conceived by combining CMA-based shape and material optimization procedures. Finally, Section VII discusses the conclusions and future work.

II. Split-ring-two-wire Nano-antenna

The split-ring-two-wire nano-antenna (SRA) hybrid was recently reported by Feichtner *et al.* [10]. The schematic diagram of the SRA structure is depicted in Fig. 1. This shape was guided by an optimization process that coupled an evolutionary algorithm with the FDTD electromagnetic solver. The process was initiated by dividing the optimization domain into 21 × 21 square pixels. Considering the current fabrication limitations the minimum feature size or the voxel size was restricted to 10 nm × 10 nm × 11 nm. Therefore, the optimization domain had an overall volume of 210 nm × 210 nm × 11 nm. The goal of the optimization was to maximize the NFIE at the center of the optimization domain (indicated by the red dot in Fig. 1) by deciding which voxels to fill with gold block and which voxels to leave empty. The NFIE magnitude can easily be increased by decreasing the minimum voxel size or by using sharp nanoscale vertices and edges [21]–[23]. However, fabrication tolerances and production costs limit the minimum voxel size and/or the use of sharp edges and vertices [24]-[25]. Therefore, during our CMA-based optimization process, we have restricted ourselves to the minimum voxel size of 10 nm × 10 nm × 11 nm and all the lateral dimensions are set to integer multiples of 10 nm.

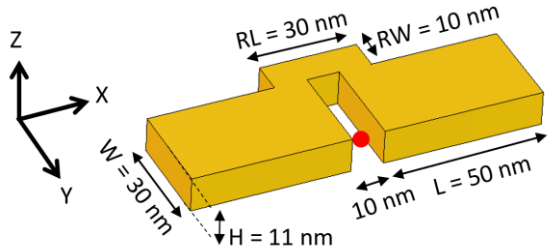

Fig. 1. 3D schematic view of Split-ring Two wire Antenna (SRA). L is along the *x*-axis, W is along the *y*-axis and H is along the *z* axis. Red-dot at the feed-gap shows the desired location of NFIE.

As can be followed from Fig. 1, the SRA has a geometry similar to a conventional nano-dipole whose two arms are connected via a bridge section (also termed as split-ring). The SRA structure is characterized with the following parameters: length of each dipole arm (*L*), width of each dipole arm (*W*), height of entire structure (*H*), length of bridge section (*RL*), width of bridge section (*RW*), and finally the gap between the two dipole arms whose value is fixed at 10 nm (as depicted in Fig. 1) to avoid quantum tunneling effects [26] and maintain current fabrication limitations [11], [24]-[25] .

As the starting point of our analysis, we will use a similar set of dimension values (Fig. 1) as reported in [10], where L = 50 nm), W = 30 nm, H = 11 nm, RL = 30 nm, and RW = 10 nm. This configuration of SRA was reported to produce a NFIE value ~ 3500 near a wavelength of 647 nm (463 THz), when illuminated with an *x*-polarized Gaussian beam simulated in a FDTD solver. We have verified the reported NFIE response with two independent commercial full-wave 3D electromagnetic solvers, namely, the Method of Moment (MOM) based FEKO[2] [27] and the Finite Element (FEM) based CST Microwave Studio [28]. To accurately model the fine geometrical details of the nano-antennas customized mesh settings were used throughout the operating frequency range from 400 THz to 550 THz (550 nm – 750 nm). In FEKO, the average edge length of the mesh triangles used was ~ 5 nm (Fig. 2a). In CST, the structures were meshed using a high frequency

[2] Certain commercial equipment, instruments, or materials are identified in this paper to foster understanding. Such identification does not imply recommendation or endorsement by the National Institute of Standards and Technology, nor does it imply that the materials or equipment identified are necessarily the best available for the purpose.

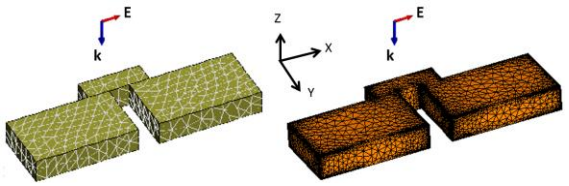

(a) (b)

Fig. 2. Mesh view of SRA as obtained from (a) FEKO triangular surface meshing and (b) CST tetrahedral mesh. The incident plane wave is propagating in the negative *z*-direction with *x*-polarized electric field.

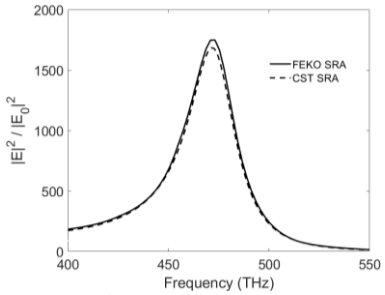

Fig. 3. Comparing NFIE of gold SRA with x-polarized plane wave excitation with two different full-wave EM solvers (FEKO and CST). Design parameters are as follows: L = 50 nm, W = 30 nm, H = 11nm, RL = 30nm, RW = 10nm.

adaptive tetrahedral mesh with maximum edge length of 3 nm (Fig. 2b). The waist size of the Gaussian beam used originally in [10] was wide enough to cover the entire SRA structure, which ensures uniform illumination over the SRA surface. In our present study, we have opted for a simple plane wave excitation uniformly illuminating the SRA. The propagating wave direction and electric field polarization are depicted in Fig. 2. Frequency-dependent material properties of gold has been incorporated into the simulations by using an interpolated version of the complex permittivity profile obtained from the experimentally-measured optical constants of gold [29]. Feichtner *et al.* have used a similar kind of curve-fitted model given in [30], based on the data from [29].

The NFIE ($|E|^2/|E_0|^2$) profiles of gold SRA obtained from FEKO and CST are compared in Fig. 3, calculated at the red dot location as shown in Fig. 1. The nano-structure was found to resonate near 472 THz. The close agreement between the independent results from FEKO and CST indicates the accuracy of the present NFIE calculations. A blue-shift of ~ 2 % in resonant frequency was observed while comparing FEKO/CST results (472 THZ) with the reported results (463 THz) [10]. Moreover, the NFIE magnitude in the present calculation is ~1800 whereas the reported value was ~3500 [10]. This deviation can be attributed to the difference in excitation methods (plane wave in the present case versus Gaussian beam in [10]) and the choice of electromagnetic solvers (FEKO and CST MWS in present case versus FDTD in [10]). The reliability of the simulated value for the highly sensitive near field has always been a prime question. Excellent work has been reported in this regard by Kupresak *et al.* in [31], where they have compared the plasmonic resonances, scattering cross section, and near-field values of nano-antennas calculated by Mie theory versus the values obtained from commercial electromagnetic solvers based on FEM, MOM and FDTD methods, which clearly shows that not all EM solvers are able to produce the same level of accuracy.

Since FEKO and CST show good agreement with each other (Fig. 3), we will carry out further optimization processes using MOM based FEKO and verify the results against the FEM-based CST solver. In the following section, we will briefly review the theory of CMA.

III. Review of Characteristic Mode Analysis

Due to its computational efficiency, we have chosen the surface integral equation (SIE) approach to perform CMA of the plasmonic nano-antennas [32]. The impedance matrix of the nano-antenna is generated using FEKO's surface equivalent principle (SEP) based MOM solver that uses the Poggio–Miller–Chan–Harrington–Wu (PMCHW) formulations [33]. The accuracy of FEKO's MOM matrix in performing CMA of nanostructures has been reported previously [18]-[19]. An in-house code, developed based on the CMA procedure outlined in [33]–[37], was used for necessary post-processing of the FEKO generated MOM matrix. The post-processing of the impedance matrix involves the application of Galerkin's MOM formulation on PMCHW integral equation that establishes a system of equations containing the partitioned impedance matrix, the equivalent surface electric and magnetic currents $\boldsymbol{J}$ and $\boldsymbol{M}$, and the vectors proportional to the incident electric and magnetic fields $\boldsymbol{V^E}$ and $\boldsymbol{V^H}$ [38]:

$$\begin{bmatrix} Z^{EJ} & Z^{EM} \\ Z^{HJ} & Z^{HM} \end{bmatrix} \begin{bmatrix} \boldsymbol{J} \\ \boldsymbol{M} \end{bmatrix} = \begin{bmatrix} \boldsymbol{V^E} \\ \boldsymbol{V^H} \end{bmatrix} \tag{1}$$

where Z^{EJ} and Z^{HJ} are the MOM impedance matrix partitions that link the electric currents $\boldsymbol{J}$ to $\boldsymbol{V^E}$ and $\boldsymbol{V^H}$, respectively, and Z^{EM} and Z^{HM} are the MOM impedance matrix partitions that link the magnetic currents $\boldsymbol{M}$ to $\boldsymbol{V^E}$ and $\boldsymbol{V^H}$, respectively. This set of linear equations can be re-formulated to express the induced magnetic current equivalently as,

$$\boldsymbol{M} = [Z^{HM}]^{-1}[\boldsymbol{V^H} - Z^{HJ}\boldsymbol{J}] \tag{2}$$

Substituting (2) back into (1) yields a new relation between the induced electric current $\boldsymbol{J}$ and the external excitations through a new symmetric impedance matrix Z^E,

$$[Z^E][\boldsymbol{J}] = \boldsymbol{V^E} - Z^{EM}[Z^{HM}]^{-1}\boldsymbol{V^H} \tag{3}$$

where Z^E is given by

$$Z^E = Z^{EJ} - Z^{EM}[Z^{HM}]^{-1}Z^{HJ} \tag{4}$$

Applying CMA to Z^E, a new generalized eigenvalue problem can be formed:

$$X^E(\boldsymbol{J_n}) = \lambda_n R^E(\boldsymbol{J_n}) \tag{5}$$

where the subscript n signifies the mode numbers, λ_n are the eigenvalues, and $\boldsymbol{J_n}$ are the eigenvectors or fundamental eigenmodes/eigencurrents of the structure. The terms R^E and

This article has been accepted for publication in a future issue of this journal, but has not been fully edited. Content may change prior to final publication. Citation information: DOI 10.1109/TAP.2019.2938705, IEEE Transactions on Antennas and Propagation

X^E are the real and imaginary parts of the equivalent MOM impedance matrix Z^E, respectively, which are frequency-dependent, and thus it becomes necessary to solve (5) to yield a new set of λ_n and $\boldsymbol{J_n}$ at every solution frequency.

The equivalent surface electric current ($\boldsymbol{J}$) on the scatterer can be expressed as a weighted sum of its eigenvectors or eigenmodes [32]:

$$\boldsymbol{J} = \sum_n a_n \boldsymbol{J_n} = \sum_{\boldsymbol{n}} \frac{V_n \boldsymbol{J_n}}{(1 + j\lambda_n)} \tag{6}$$

The term V_n is the modal excitation coefficient (MEC), which defines the coupling between the impressed electric field and the n[th] eigenmode:

$$V_n = < \boldsymbol{J_n}, \boldsymbol{E^i} > = \iint \boldsymbol{J_n} \cdot \boldsymbol{E^i}\, ds \tag{7}$$

The magnitude of the inverse of the denominator in (6) is defined as the Modal Significance (MS_n) of the n^{th} mode, whose dimensionless value always lies between 0 and 1:

$$MS_n = \frac{1}{|1 + j\lambda_n|} \tag{8}$$

The smaller the value of λ_n, the higher the value of MS_n, and the more significant the mode becomes at a particular frequency. The modal significance (MS_n) is independent of the incident excitation, and it depends only on the properties of scattering object (e.g., shape, size, and material) and its environment. The modal excitation coefficient (V_n) encapsulates the entire dependency on the incident field excitation. Decomposing the surface equivalent electric current ($\boldsymbol{J}$) of the nano-antenna, as in (6), into terms that are independent of the incident excitation, (MS_n), and terms that depend on the incident excitation, (V_n), facilitates the nano-structure optimization process, as will be detailed in the following sections. Readers should note that from here onwards, all the diagrams showing MS_n variations and eigencurrent patterns are generated by our in-house CMA algorithm whereas the near-field value and total surface currents are obtained from FEKO. The details are also given within each figure caption.

IV. CMA Based Shape Optimization of Nano-antennas

In the following subsections, we will discuss the process of SRA shape optimization using the CMA technique to enhance the induced near field around 472 THz at the desired location near SRA (red dot in Fig. 1). This optimization differs from the previously reported study in [10], since we are utilizing the CMA as the decision making tool in the process of optimization and using a plane wave excitation instead of a Gaussian beam.

A. Finding the dominant SRA eigenmode at a desired frequency

We first calculate the modal significance, MS_n, for gold SRA and compare its response against PEC SRA, both having identical dimensions as in Fig. 1. CMA information is extracted by post-processing the FEKO-generated impedance matrix Z^E with our in-house CMA algorithm. We consider the frequency range from 154 THz to 550 THz (545 nm – 2000 nm) for the gold SRA, which partly covers the visible spectrum as well as the infra-red spectrum. For PEC SRA this range is moved to 100 THz to 4000 THz. Figs. 4a and 4b. depict the modal significance of first three dominant eigenmodes for gold SRA and PEC SRA with large modal significance values. The first mode of gold SRA, M1 in Fig. 4a, resonates at 237 THz with a peak value of $MS_1 \approx 1$. The MS_n profiles for the second and third mode (M2 and M3 respectively) almost overlap, resonating near 483 THz. M2 and M3 are insignificant near 237 THz, as $MS_2 \approx MS_3 \approx 0$ in that region. From 450 THz to 500 THz, M2 and M3 show higher modal significance than M1 and therefore M2 and M3 will have higher chances to dominate the total current response $\boldsymbol{J}$ induced on the SRA surface as well as the NFIE response in this frequency range.

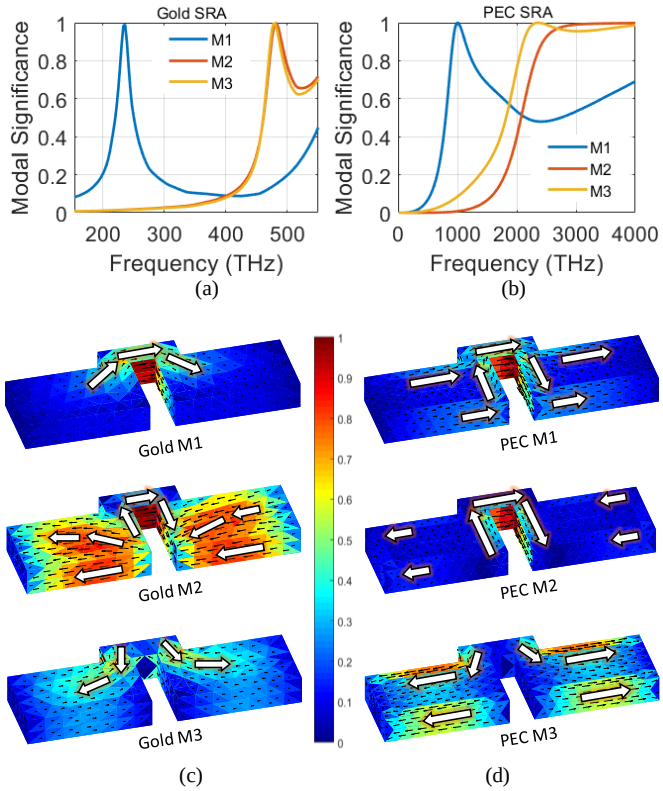

Fig. 4. Modal significance of first three significant eigen modes of (a) gold SRA and (b) PEC SRA. Normalized eigen current patterns at their respective mode resonant frequencies for (c) gold SRA and for (d) PEC SRA. All design parameters are same as in Fig. 1. Solution generated by in-house CMA algorithm.

It is clear from Fig. 4a and Fig. 4b that the values of the MS_n coefficients of the PEC SRA are significantly different from those of the gold SRA. Gold and similar noble metals behave more like lossy dielectrics in the visible spectrum. The mode resonances for the gold SRA appear below 500 THz, whereas the PEC modes start resonating beyond 1000 THz. This is due to the difference in velocity factors between PEC and gold [39]. The MS_n resonances of the gold SRA not only shift to lower frequencies, but their bandwidths become narrower, unlike PEC

This article has been accepted for publication in a future issue of this journal, but has not been fully edited. Content may change prior to final publication. Citation information: DOI 10.1109/TAP.2019.2938705, IEEE Transactions on Antennas and Propagation

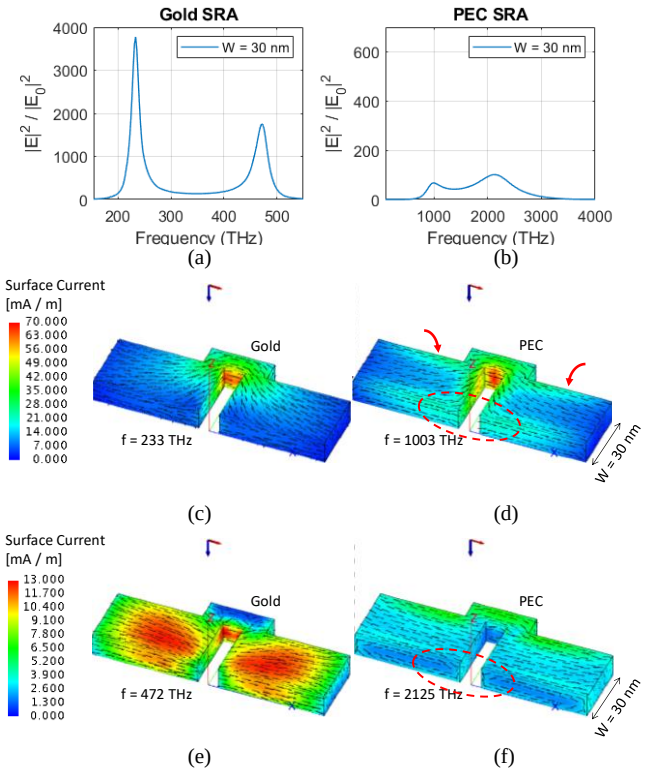

Fig. 5. NFIE response of (a) gold SRA and (b) PEC SRA with identical dimensions as in Fig. 1. Total surface current distribution corresponding to first near-field resonance for (c) gold SRA at 233 THz and (d) for PEC SRA at 1003 THz. Total surface current distribution corresponding to second near-field resonance for (e) gold SRA at 472 THz and (f) for PEC SRA at 2125 THz. Results obtained using FEKO.

antennas, which show wideband modes. Therefore, the material of a nano-antenna changes the resonant frequencies of the modes and their bandwidths affect the mode mixture at each frequency. For example, at the resonant frequency of Mode 2 of the gold SRA, the modal significance of the first three modes is {0.15, 1.0, 1.0} whereas at the resonant frequency of Mode 2 of the PEC SRA, the modal significance of the first three modes is {0.5, 1.0, 0.95}.

Fig. 4c and Fig. 4d depict the normalized eigencurrent patterns for the gold and PEC SRAs, respectively, generated by our in-house CMA algorithm. The eigenmodes exhibit slight variations with frequency and so each mode is plotted at its corresponding resonant frequency. The color bar refers to the normalized scale for each individual mode, where red defines the maximum normalized current strength of 1 and blue defines the minimum normalized current strength of 0. The direction of the currents are highlighted with white arrows.

The eigencurrent pattern of mode M1 for the gold SRA (Fig. 4c), is mostly confined in the vicinity of the bridge connecting the two dipole arms. In contrast to that, the eigencurrents for M2 are found to be strongly distributed over the dipole arms that are flowing in phase with each other but 180° out of phase with the split ring current flow. For M3, the eigencurrents start flowing from the split ring section and spread uniformly into the dipole arms but in opposite directions.

The eigencurrent distribution of the PEC SRA modes are significantly different from that of the gold SRA modes, as

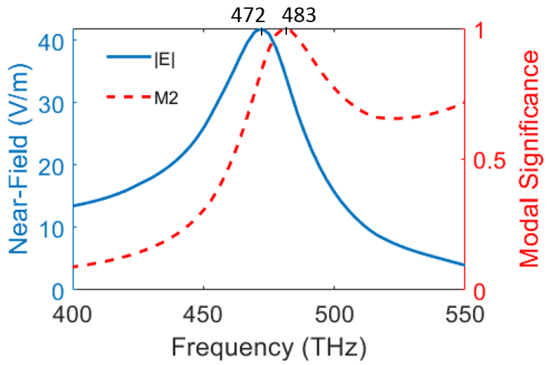

Fig. 6. Comparison between near-field resonance as obtained from FEKO and eigenmode resonance as obtained from in-house CMA algorithm for a gold SRA with dimension as in Fig. 1. Blue curve shows the near-field resonance and corresponding magnitude is labeled in *y*-axis on the left hand side. Red curve shows the modal significance of eigenmode M2 and corresponding magnitude is labeled in *y*-axis on the right hand side.

evident from the comparison between Fig. 4c and Fig. 4d, even though they show the same directional trends. The infinite conductivity of the PEC SRA causes the eigencurrents to show maxima near the sharp edges of the structure as observed in Fig. 4d. However, Fig. 4c shows that the eigencurrents of the gold SRA are more uniformly distributed and, therefore, do not exhibit maxima at the edges. These differences in the eigencurrent distribution along with their different modal significance values will lead to significant differences in the total current excited on the SRA and ensuing NFIE.

We plot the NFIE and the total surface current pattern ($\boldsymbol{J}$) for the gold and PEC SRA as shown in Fig. 5. For both the gold and PEC cases, $\boldsymbol{J}$ is plotted at their respective NFIE resonant frequencies. The plots of $\boldsymbol{J}$ and NFIE are obtained from the FEKO simulations where each SRA is illuminated with a normally incident $\boldsymbol{x}$ - polarized plane wave $\boldsymbol{E^i}$. A comparison between Fig. 5c and Fig. 4c gold M1 mode clearly shows that M1 dominates the total current response of the gold SRA at the first near-field resonant frequency (233 THz). This is because the gold M1 mode is the only significant mode near 233 THz (Fig. 4a) whose eigencurrents in the bridge section can couple strongly to the incident electric field $\boldsymbol{E^i}$, leading to a high value of V_1 (MEC of M1) following (7). A similar explanation holds for the total current response of the gold SRA at second near-field resonant frequency (472 THz) (Fig. 5e), which closely matches that of the 2nd eigenmode (Fig. 4c, M2). In this case also, we find a high value of V_2 according to (7), since the incident field $\boldsymbol{E^i}$ now couples strongly with the in-phase dipole arm currents of M2, which along with the high value of MS_2 near 472 THz makes M2 the strongest mode to dominate the total current response for the gold SRA.

However, despite being a significant mode at 472 THz, the gold M3 mode is not expressed in the total surface current since it is unable to couple to the incident field $\boldsymbol{E^i}$. This is because the M3 gold eigencurrent is flowing in opposite directions on the two dipole arms (Fig. 4c, gold M3). Therefore, when evaluating the integral for V_3 in (7) over the surface of the gold SRA, the contribution of surface currents from the right hand side dipole arm will cancel the contribution from the left hand side dipole arm, causing V_3 to nearly vanish [18]–[19]. This study shows

This article has been accepted for publication in a future issue of this journal, but has not been fully edited. Content may change prior to final publication. Citation information: DOI 10.1109/TAP.2019.2938705, IEEE Transactions on Antennas and Propagation

that the expression of a mode in the total induced surface current depends on both the MS_n and V_n parameter values. At frequencies between the two resonances (e.g. 300 – 400 THz), the total current is a mixture of all modes, since in this range the values of MS_n and V_n for different modes are comparable to each other.

A comparison between Fig. 5a and Fig. 5b shows that the NFIE of the PEC SRA is significantly smaller than that of the gold SRA (notice the difference in the scale used for the y-axis in both subplots). Also, Fig. 5b shows that the PEC NFIE's second resonance is higher in magnitude than the first resonance, which is opposite to the behavior observed in the gold SRA. These differences between the NFIE of the gold and the PEC SRAs can be attributed to the differences between the $\boldsymbol{J}$ of the PEC and the $\boldsymbol{J}$ of the gold SRA as shown in Fig. 5c-5f. In particular, we have highlighted the edges of the PEC SRA in Fig. 5d exhibiting current maxima, which are absent from the gold SRA (Fig. 5c). In Fig. 5f the red circle highlights the circulating total current near PEC SRA feed edge which are absent from gold SRA in Fig. 5e. The results in Fig. 4 and Fig. 5 show the effect of the material composition on the electromagnetic response of the SRA and highlight that the behavior of a PEC nano-antenna differs significantly from that of a nano-antenna composed of a realistic metal like gold or silver, and thus the optimization strategy will be different in these two different scenarios.

Since FEKO better interpolates the color shadings, the current plots in Fig. 5c-5f appears smoother compared to plots in Fig. 4c-4d, which are generated by our in-house CMA algorithm. However, the Fig. 4 and Fig. 5 current plots are both derived from the same impedance matrix generated by the FEKO MOM solver. These close similarities between the total surface current and eigencurrent patterns are sufficient to identify the dominant mode at a particular frequency.

B. Shape optimization based on eigenmode behavior

Our objective in this section is to improve NFIE response of gold SRA near 472 THz with $\boldsymbol{x}$ - polarized plane wave excitation. Our strategy is to first identify the eigenmode responsible for the near field resonance and then focus on improving its effects. Fig. 5e clearly shows that the total current on gold SRA at 472 THz is dominated by the gold M2 mode. Fig. 6 shows the close proximity between the modal significance of M2 and the near field value within the 450 THz to 550 THz range. There is only ~ 2 % shift between the eigenmode resonance of M2 (483 THz) and the corresponding near field resonance (472 THz). This shift can be attributed to the fact that M2 is the modal significance of the entire SRA structure, whereas the near field is evaluated at only one specific point (red dot in Fig. 1). Since gold M2 is the only dominant mode near 472 THz and is able to strongly couple to the incident $\boldsymbol{x}$ - polarized plane wave excitation, our focus will be on strengthening this coupling further by means of gold SRA shape optimization to pursue the ultimate goal of near-field enhancement. This can be done by controlling the two independent parameters, MS_2 and V_2.

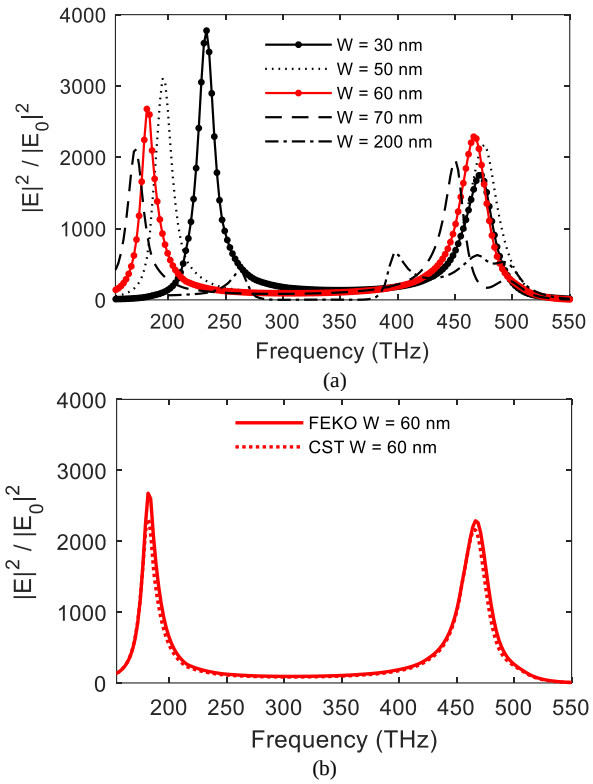

Fig. 7. (a) NFIE response as obtained from FEKO for gold SRA with different values of W. (b) Verifying FEKO solution against CST for W = 60 nm shape optimized gold SRA. Remaining parameters are same as in Fig. 1.

To enhance the expression of M2 in the total current $\boldsymbol{J}$ in (6), either MS_2 or V_2 or both can be increased. Already, at 483 THz, MS_2 has the maximum value of unity and therefore it cannot be increased further. Preserving this condition, we still can improve V_2 by increasing the surface area of the dipole arms of the gold SRA where M2 is strong in magnitude. This will increase the area of the integral in (7), increasing the coupling of the incident field to the structure and in turn the value of V_2. This is true when the *x*-polarized electric field $\boldsymbol{E^i}$ is uniform over the plane of the gold SRA, which happens in the case of normal incidence. We also assume that the eigencurrent pattern of $\boldsymbol{J_2}$ remains approximately the same as in Fig. 4c. We will check the second assumption later.

The surface area of the SRA dipole arms can be increased in three ways, either by increasing *L* or *W* or both. Changing *L* or *W* will change the aspect ratio of the structure, which can potentially shift the resonant frequency [2]. Our goal is to increase the near field value while keeping the resonant frequency unchanged. Inspecting Fig. 4c, we find that the dimension *L* is parallel to the direction of the gold M2 eigencurrent. Therefore, increasing *L* will red-shift the modal resonant frequency of gold M2 from 483 THz. Thus, we keep the value of *L* unchanged (50 nm) and instead *W* is increased successively in steps of 10 nm to manifest the increment in the surface area.

Fig. 7a shows the NFIE response obtained from FEKO for five different values of *W*, starting from its initial value of 30 nm up to 200 nm (since the total optimization space is limited to 210 nm × 210 nm). As we can see, the variation in *W* changes

the NFIE's second resonant frequency slightly but still all the curves resonate near 472 THz. This is because the second resonant frequency is less sensitive towards the *W* dimension since the *W* direction is perpendicular to the direction of the M2 eigencurrent. The largest NFIE is achieved at *W* = 60 nm (Fig. 7a, red curve), which surpasses the NFIE of the original SRA (*W*=30 nm), by 31 %. This is achieved near a frequency of 468 THz which is only 0.84 % red-shifted from the desired near-field resonance of 472 THz. This result was again verified in CST MWS (Fig. 7b), which shows excellent agreement with the FEKO optimized design.

To explain why *W* = 60 nm becomes the optimum value and why further increments in *W* resulted in degradation of near field performance, we have compared three cases of gold SRA M2 eigencurrent patterns: *(i)* the original SRA with *W* = 30 nm (Fig. 8a), *(ii)* the optimum SRA with *W* = 60 nm (Fig. 8b), and *(iii)* the SRA with largest possible value of *W* = 200 nm (Fig.8c). We observe that for values up to *W* = 60 nm, the M2 eigencurrent pattern remains similar to that exhibited by the original SRA structure (*W* = 30 nm), and only one maximum, a red region, occurs in the dipole arms of the SRA as shown in Fig. 8a and Fig. 8b. With further increments in *W*, the eigenmode pattern starts to exhibit multiple maxima with opposite directions of currents along the dimension *W*, as shown in Fig. 8c. Since these maxima are opposite in direction, their contribution to the integral in (7) are also of opposite sign, causing the value of $\boldsymbol{V_2}$ to drop and the near field strength to decrease. Moreover, the eigencurrent M2, which was predominantly aligned with the *x*-axis (Fig. 8a), gradually becomes aligned with the *y*-axis (Fig. 8c) as *W* reaches its maximum. Therefore, the coupling of M2 eigencurrents with the *x*-polarized incident electric field decreases significantly.

So far, in this section we have focused on the second resonance in the NFIE, which occurs around 472 THz for the gold SRA. However, it is also interesting to study the first resonance in the NFIE, which occurs around 233 THz for the *W* = 30 nm gold SRA (Fig. 7a). Unlike the second resonance, increasing *W* monotonically red-shifts the first resonant frequency location. The first NFIE resonance is dominated by M1, as shown in Fig. 5c, which is sensitive to the *W* dimension. The successive increments in *W* cause the effective electrical length of current path corresponding to M1 increase and resonant frequency decrease. The peak amplitude also reduces for the first NFIE resonance with increasing *W*. This is because the M1 eigencurrent distribution does not have maxima in the SRA arms (Fig. 4c, gold M1), so that increasing the width of the arms does not help the coupling to mode M1, which dominates the response at the first NFIE resonance.

To highlight the effect of the material on the NFIE of a nano-antenna, Fig. 9 shows the variation in the NFIE response of the gold SRA and the PEC SRA due to an identical increase in *W* from 30 nm to 60 nm. Opposite to the gold SRA, Fig. 9b shows that for the PEC SRA this increase in *W* will cause the first resonance of the NFIE to increase its peak amplitude and the second resonance to decreases its peak amplitude. This difference in behavior between the gold and the PEC SRA can also be attributed to the differences in the eigencurrent distribution shown in Fig. 4.

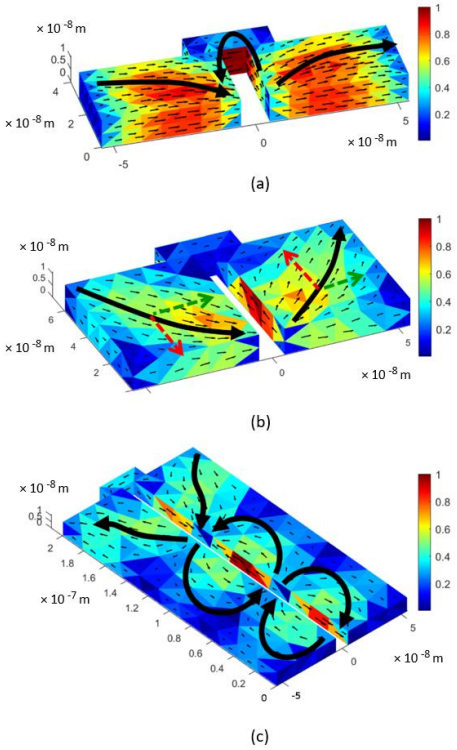

Fig. 8. Enhancing incident field coupling to gold SRA by studying eigencurrent behavior (near 483 THz). (a) Mode 2 eigencurrent pattern with W=30 nm, (b) modified eigencurrent of Mode 2 with W=60 nm and (c) repetition in current maxima-minima as observed in SRA with W=200 nm. Rest of the parameters are same as in Fig. 1. (Solution generated by in-house CMA algorithm.)

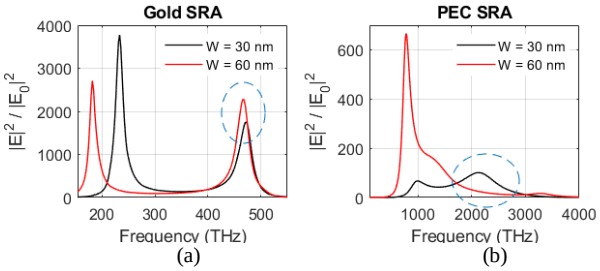

Fig. 9. Comparison of NFIE response in (a) gold SRA and in (b) PEC SRA with *W* = 30 nm and 60 nm. Results obtained using FEKO. Remaining parameters are same as in Fig. 1.

In summary, CMA can be used to optimize the NFIE response by identifying the modes that contribute to each near-field resonance and by showing the current distribution of each mode for nano-antennas with different materials. The knowledge of the current distribution of these modes can be used to identify which dimensions of the nano-antenna to optimize. Therefore, CMA gives physical insight into the problem and so leads the optimization process in the right direction. This is where the CMA approach differs from other computationally expensive search algorithms, where the nano-antenna shapes are optimized using trial and error methods.

V. Impact of Material Properties on Eigenmode Behavior

A proper choice of material plays an important role in achieving the desired plasmonic effects when the operating frequency is predefined [3], [40]-[41]. We consider two noble metals, gold (Au) and silver (Ag), whose relative complex permittivity profiles are shown in Fig. 10a (real part) and Fig. 10b (imaginary part), as obtained from the Johnson and Christy experimental data reported in [29]. Fig. 11 compares the modal significance profiles of two identical dimension SRAs composed of gold or silver (dimensions as in Fig. 1), so that if any changes occur in the modal behavior that will be due to material changes only. Significant differences are observed between the gold and silver modes. All the silver modes resonate at higher frequencies compared to the gold modes, and they also have narrower bandwidths. Moreover, Fig. 11 shows that all the silver modes exhibit sharp distinct resonances, where the MS_n values reach their maximum first and then decrease monotonically with increasing frequency. However, the MS_1 profile for gold SRA shows a resonance at 237 THz, followed by a decrease in magnitude until approximately 450 THz, and then again increasing until it saturates to a value of unity. A similar kind of rise in magnitude is found for the MS_2 and MS_3 coefficients for the gold SRA beyond 500 THz, following their resonances near 483 THz. These differences can be explained as follows:

1) Plasmonic Resonance

The occurrence of plasmonic resonances in a nanostructure depends on its size, material, and environment, which altogether define a real negative value of the relative dielectric permittivity of the constituent material required to create a resonance condition. To produce a plasmonic resonance in the SRA structure in free-space, with dimensions as stated in Fig. 1, the required value was found as $Re(\varepsilon) \sim -12$ (indicated by a horizontal dash-dot line in Fig. 10a). The gold SRA reaches this required value of $Re(\varepsilon)$ near 472 THz, whereas the silver SRA reaches this value near 565 THz. Due to this difference, silver nanostructures resonate at higher frequencies than their gold counterparts.

2) Plasmonic quality factor

The narrower resonances of the silver SRA can be explained in terms of the plasmonic quality factor, which is inversely related to the resonance bandwidth, defined as the negative ratio of the real part of permittivity to the imaginary part of permittivity [42],

$$Q(\omega) = -\frac{Re[\varepsilon(\omega)]}{Im[\varepsilon(\omega)]} \tag{9}$$

From Fig. 10a and Fig. 10b, it is evident that for a fixed frequency value,

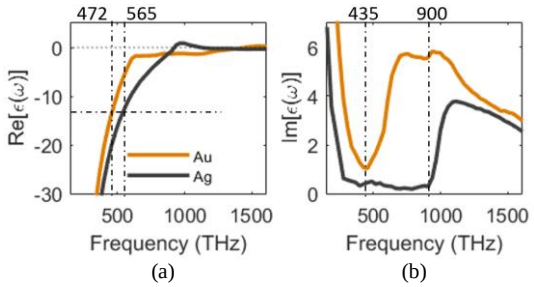

(a) (b)

Fig. 10. Frequency dependent interpolated complex permittivity data for gold and silver computed using experimental optical constants as reported by Johnson and Christy [29].

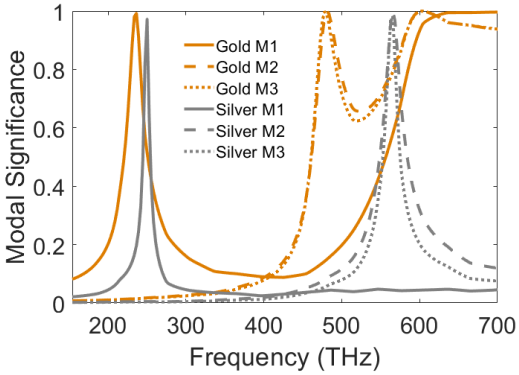

Fig. 11. Study of modal significance behavior of first three significant modes of gold SRA and silver SRA. All design parameters are same as in Fig. 1, and solved with in-house CMA algorithm.

$$-Re[\varepsilon_{silver}(\omega)] > -Re[\varepsilon_{gold}(\omega)]$$
$$Im[\varepsilon_{silver}(\omega)] < Im[\varepsilon_{gold}(\omega)]$$

Consequently from (9) we get,

$$Q_{silver}(\omega) > Q_{gold}(\omega)$$

Thus, the silver SRA modes have higher quality factors and therefore narrower bandwidths compared to the corresponding gold SRA modes.

3) Inter-band transition effects

The rising trend in the modal significance plot in Fig. 11 for gold SRA modes beyond 500 THz is related to the inter-band transition phenomena that occur in both gold and silver plasmonic materials [43]–[45]. As shown in Fig. 10b, the imaginary part of the complex permittivity, for both gold and silver, decays monotonically starting from very low frequency till approximately 435 THz, as marked by the first vertical dashed line. Beyond that region, inter-band transitions initiates in gold and increases material losses, resulting in an increase of $Im[\varepsilon_{gold}(\omega)]$. This increase in the imaginary part of the complex permittivity is reflected in the gold SRA modes in Fig. 11 as a rise in the modal significance value of the modes beyond their resonant frequency. But for silver, the inter-band transition region is located in the ultra-violet range, beyond 900 THz (3.7 eV) [43], marked by the second vertical dashed line in Fig. 10b. Since the current operating frequency range is limited to 700

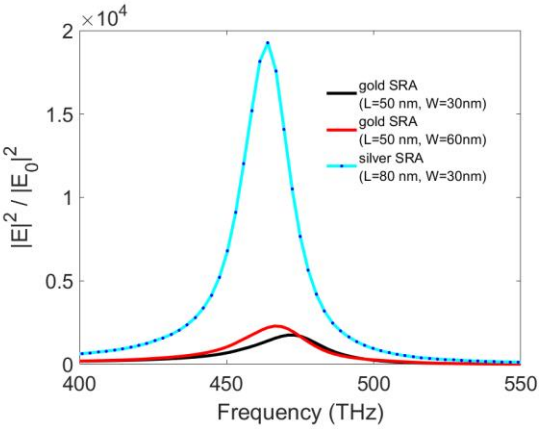

Fig. 12. Combination of shape and material optimization, showing a comparison among the normalized near-field enhancement as obtained from FEKO for gold SRA with L=50 nm, W=30 nm (black curve); gold SRA with L=50 nm, W=60 nm (red curve) and silver SRA with L=80 nm, W=30 nm (cyan curve). All other design parameters are same as in Fig. 1.

THz, the rising phenomena of silver SRA modes did not appear in Fig. 11.

This analysis helps us to understand the plasmonic response from the viewpoint of material characteristics. The correlation between modal behavior and the complex permittivity model characterizing the material can play a critical role in choosing the optimum material for any frequency-specific plasmonic application. This general statement will be elaborated in the following section.

VI. Plasmonic Material Optimization Based on CMA

So far we have discussed how to independently optimize either the shape or the material of nano-antennas by studying their modal behavior response. In section IV, we achieved a 31% improvement in the NFIE value for the gold SRA by optimizing its shape with CMA information. But one can generate a much higher value of NFIE if the nano-antenna shape as well as the material are optimized together following the eigenmode response. One such outstanding NFIE response is shown in Fig. 12 (cyan curve), achieved by simultaneously optimizing the shape and material of an SRA designed to resonate near 472 THz. The steps for this dual-optimization process are as follows:

1. As silver shows enhanced material properties compared to gold, our idea was to re-design the SRA with silver material.
2. With the dimensions as in Fig. 1, the silver SRA was observed to produce its second eigenmode resonance near 565 THz (Fig. 11), which is the preferred mode to produce a high NFIE value under an *x*-polarized incident electric field.
3. To make the silver SRA NFIE resonate near 472 THZ, it was required to redshift the silver M2 resonance from 565 THz towards 472 THz and this was achieved by increasing the aspect ratio (L/W) of the silver SRA structure.
4. The strategy of decreasing W was discarded since it would decrease the surface area exposed to the incident electric field resulting in a decrease in the V_2 value according to (7).
5. Therefore, the W value was kept fixed at 30 nm, and the value of L was increased in steps of 10 nm.
6. The CMA shows that increasing L is the optimum choice to red-shift the second eigenmode resonance of the silver SRA, since the currents of M2 are parallel to the L dimension. Moreover, an increase in the L dimension eventually increases the surface area of integration in (7), resulting in a better coupling of the incident field to the structure.

This optimization process was continued until the resonant frequency fell within 2 % of the desired value of 472 THz. The final optimized silver SRA satisfying the resonant frequency condition was found to have L = 80 nm and W = 30 nm. Fig. 12 compares three NFIE profiles as follows: (1) gold SRA with the original dimensions as in [10] (L = 50 nm and W = 30 nm), (2) the CMA-based shape optimized gold SRA with dimensions (L = 50 nm and W = 60 nm), and (3) finally the CMA based shape and material optimized silver SRA with dimensions (L = 80 nm and W = 30). The optimized silver SRA resonates near 464 THz which is only 1.9 % red-shifted from the desired frequency of 472 THz of the original gold SRA. This optimized silver SRA (cyan curve) produces an extremely high NFIE value that surpasses the value of the shape optimized gold SRA (red curve) by ~ 700 %, and exceeds the original gold SRA (black curve) by ~ 1000 %. This superior NFIE response is due to the superior silver permittivity profiles.

The enhanced performance of silver was anticipated, and it has already been reported in several studies [41],[46]. But the analysis was carried out intentionally to show a different aspect of CMA that works efficiently for joint shape and material optimization in achieving a desired plasmonic response within a specific set of requirements.

VII. Conclusion

This paper provides general guidelines to understand and optimize complex plasmonic nano-antenna problems with the aid of Characteristic Mode Analysis (CMA). The near field enhancement process of a split-ring two-wire antenna (SRA) has been demonstrated using this technique. CMA provides the modal significance of the excitation-independent eigenmodes at each frequency and plots corresponding eigencurrent patterns. The dominant eigenmode responsible for near-field resonance is then identified by a detailed comparison of the total surface current pattern with respect to the significant eigenmode patterns. Guided by these CMA insights, the dimensions of the SRA are then modified to enhance the incident field coupling with the dominant mode, which results in enhancement in the SRA near-field value. This paper also describes the correlation between the inter-band transition phenomena of plasmonic materials and the behavior of the eigenmodes of a plasmonic nano-antenna. Based on CMA information, we further optimize both the shape and material of the SRA which yields 700 – 1000 % enhancement of the normalized near field intensity. The general CMA optimization approach developed in this study should find a wide range of potential applications involving synthesizing nano-antennas for enhanced plasmonic response.

REFERENCES

[1] H. A. Atwater and A. Polman, "Plasmonics for improved photovoltaic devices". *Nature Mater.* vol. 9, pp. 205–213, Mar. 2010. doi: 10.1038/nmat2629

[2] J. A. Schuller, E. S. Barnard, W. Cai, Y. C. Jun, J. S. White and M. L. Brongersma, "Plasmonics for extreme light concentration and manipulation. *Nature Mater.* vol. 9, pp. 193–204, Mar. 2010. doi: 10.1038/nmat2630

[3] S. A. Maier, *Plasmonics: Fundamentals and Applications*. New York, NY, USA: Springer, 2007.

[4] P. Mühlschlegel1, H.-J. Eisler , O. J. F. Martin, B. Hecht, and D.W. Pohl, "Resonant Optical antennas" *Science*, vol. 308, 1607-1609, 2005. Doi: 0.1126/science.1111886

[5] P. J. Schuck, D. P. Fromm, A. Sundaramurthy, G. S. Kino and W. E. Moerner, "Improving the Mismatch between Light and Nanoscale Objects with Gold Bowtie Nanoantennas" *Phys. Rev. Lett.*, vol. 94, pp. 017402, 2005. Doi: 10.1103/PhysRevLett.94.017402.

[6] C. Forestiere, M. Donelli, G. F. Walsh, E. Zeni, G. Miano, and L. D. Negro, "Particle-swarm optimization of broadband nanoplasmonic arrays". *Opt. Lett.* vol. 35, no. 2 pp. 133-135, Jan. 2010.

[7] C. Forestiere, A. J. Pasquale, A. Capretti, G. Miano, A. Tamburrino, S. Y. Lee, B. M. Reinhard, and L. D. Negro, "Genetically Engineered Plasmonic Nanoarrays" *Nano. Lett.* vol. 12, pp. 2037-2044, 2012. Doi: 10.1021/nl300140g.

[8] P. Ginzburg, N. Berkovitch, A. Nevet, I. Shor, and M. Orenstein, "Resonances On-Demand for Plasmonic Nano-Particles" *Nano. Lett.* vol. 11, pp. 2329-2333, 2011. Doi: 10.1021/nl200612f.

[9] D. Macías , P. -M. Adam, V. Ruíz-Cortés , R. Rodríguez-Oliveros , and J. A. Sánchez-Gil , "Heuristic optimization for the design of plasmonic nanowires with specific resonant and scattering properties" *Opt. Express.* vol. 10, no. 2, pp. 13146-13163, 2012.

[10] T. Feichtner, O. Selig, M. Kiunke, and B. Hecht, "Evolutionary Optimization of Optical Antennas", *Phys. Rev. Lett.* vol. 109, pp. 127701, 2012. Doi: 10.1103/PhysRevLett.109.127701

[11] T. Feichtner, O. Selig, and B. Hecht, "Plasmonic nanoantenna design and fabrication based on evolutionary optimization", *Opt. Express.* vol. 25, no. 10, pp. 10828-10842, 2017. Doi: 10.1364/OE.25.010828.

[12] R. Garbacz, "Modal expansions for resonance scattering phenomena," *Proc. IEEE*, vol. 53, no. 8, pp. 856–864, Aug. 1965.

[13] R. F. Harrington and J.Mautz, "Theory of characteristic modes for conducting bodies," *IEEE Trans. Antennas Propag.*, vol. 19, no. 5, pp. 622–628, Sep. 1971.

[14] M. Cabedo, E. Antonino, A. Valero and M. Ferrando, "The Theory of Characteristic Modes Revisited: A Contribution to the Design of Antennas for Modern Applications," Antennas Propag. Magazine, vol. 49, pp. 52-68, Oct. 2007.

[15] F. H. Lin and Z. N. Chen, "Low-Profile Wideband Metasurface Antennas Using Characteristic Mode Analysis," in *IEEE Trans. Antennas Propag.*, vol. 65, no. 4, pp. 1706-1713, April 2017. doi: 10.1109/TAP.2017.2671036

[16] D. Kim and S. Nam, "Systematic Design of a Multiport MIMO Antenna With Bilateral Symmetry Based on Characteristic Mode Analysis," in *IEEE Trans. Antennas Propag*, vol. 66, no. 3, pp. 1076-1085, March 2018. doi: 10.1109/TAP.2017.2787607

[17] L. Guan, D. Ding, Z. Fan, M. Li, Z. Li and R. Chen, "Analysis of dielectric resonator antennas using characteristic modes," *2016 IEEE/ACES*, Honolulu, HI, 2016, pp. 1-2. doi: 10.1109/ROPACES.2016.7465346

[18] A. M. Hassan, F. Vargas-Lara, J. F. Douglas and E. J. Garboczi, "Electromagnetic Resonances of Individual Single-Walled Carbon Nanotubes With Realistic Shapes: A Characteristic Modes Approach," *IEEE Trans. Antennas Propag*, vol. 64, no. 7, pp. 2743-2757, July 2016. doi: 10.1109/TAP.2016.2526046

[19] K. C. Durbhakula, A. Hassan, F. Vargas-Lara, D. Chatterjee, M. Gaffar, J. F. Douglas, and E. J. Garboczi, "Electromagnetic Scattering From Individual Crumpled Graphene Flakes: A Characteristic Modes Approach", *IEEE Trans. Antennas Propag*, vol. 65, no. 11, pp. 6035-6047, Nov. 2017. doi: 10.1109/TAP.2017.2752218

[20] P. Ylä-Oijala, D. C. Tzarouchis, E. Raninen and A. Sihvola, "Characteristic Mode Analysis of Plasmonic Nanoantennas," *IEEE Trans. Antennas Propag.*, vol. 65, no. 5, pp. 2165-2172, May 2017. doi: 10.1109/TAP.2017.2677921

[21] D. P. Fromm, A. Sundaramurthy, P. J. Schuck, G. Kino, and W. E. Moerner, "Gap-Dependent Optical Coupling of Single "Bowtie" Nanoantennas Resonant in the Visible" *Nano. Lett.* vol. 4, No. 5, pp. 957-961, 2004. doi 10.1021/nl049951r.

[22] J. Aizpurua and S. P. Apell, "Role of tip shape in light emission from the scanning tunneling microscope" *Phys. Rev. B.* vol. 62, no. 3, pp. 2065-2073, 2000.

[23] A. Wiener, A. I. Fernández-Domínguez, A. P. Horsfield, J. B. Pendry, and S. A. Maier, "Nonlocal Effects in the Nanofocusing Performance of Plasmonic Tips" *Nano. Lett.* vol. 12, pp. 3308-3314, 2012. Doi: 10.1021/nl301478n

[24] V. R. Manfrinato, L. Zhang, D. Su, H. Duan, R. G. Hobbs, E. A. Stach, and K. K. Berggren, "Resolution Limits of Electron-Beam Lithography toward the Atomic Scale" *Nano. Lett.* vol. 13, pp. 1555-1558, 2013. Doi:10.1021/nl304715p.

[25] M. Davanco, L. Yu, L. Chen, V. Luciani, and J. A. Liddle, "Assessing fabrication tolerances for a multilevel 2D binary grating for 3D multifocus microscopy," Opt. Express 24, 9224-9236, 2016.

[26] W. Zhu, R. Esteban, A. G. Borisov, J. J. Baumberg, P. Nordlander, H. J. Lezec, J. Aizpurua, and K. B. Crozier, "Quantum mechanical effects in Plasmonic structures with subnanometre gaps". *Nature Comm.* vol. 7, pp. 11495, June. 2016. doi: 10.1038/ncomms11495

[27] FEKO. v.14.0 *EM Simulation Software*, FEKO online: https://www.feko.info

[28] CST Microwave studio. (2016) 3D *EM Simulation Software*, CST online: https://www.cst.com.

[29] P. B. Johnson and R. W. Christy, "Optical constants of the noble metals," *Phys. Rev. B*, vol. 6, no. 12, 4370-4379, 1972.

[30] P. G. Etchegoin, E. C. Le Ru, and M. Meyer, "An analytic model for the optical properties of gold," *J. Chem. Phys. Phys.*, vol. 125, pp. 164705, 2006. DOI: 10.1063/1.2360270

[31] M. Kupresak, X. Zheng, G. A. E. Vandenbosch, and V. V. Moshchalkov, "Benchmarking of software tools for the characterization of nanoparticles," *Opt. Express*, vol. 25, no. 22, p. 26760, Oct. 2017.

[32] Y. Chang and R. F. Harrington, "A Surface Formulation for Characteristic Modes of Material Bodies," *IEEE Trans. Antennas Propag.*, vol. 20, no. 2, pp. 194–198, Mar. 1977.

[33] Y. K. Chen and C. F. Wang, "Surface Integral Equation Based Characteristic Mode Formulation for Dielectric Resonators," Antennas Propag. Soc. Int. Symp. (APURSI), 2014 IEEE, pp. 846-847. doi: 10.1109/APS.2014.6904751.

[34] R. F. Harrington and J. Mautz, "Computation of characteristic modes for conducting bodies," *IEEE Trans. Antennas Propag.*, vol. 19, no. 5, pp. 629–639, Sep. 1971.

[35] S. M. Rao, D. R. Wilton, and A. W. Glisson, "Electromagnetic scattering by surfaces of arbitrary shape," *IEEE Trans. Antennas Propag.*, vol. 30, no. 3, pp. 409–418, May 1982.

[36] W. C. Gibson, *The Method of Moments in Electromagnetics*. London, U.K.: Chapman & Hall/CRC Press, 2008.

[37] B. D. Raines and R. G. Rojas, "Wideband Characteristic Mode Tracking," IEEE Trans. Antennas Propag., vol. 60, pp. 3537-3541, July. 2012.

[38] Y. Chen and C. Wang, *Characteristic Modes: Theory and Applications in Antenna Engineering*, Wiley, Jun 2015, ISBN: 978-1-119-03842-9.

[39] J. Dorfmuller, R. Vogelgesang, W. Khunsin, C Rockstuhl, C. Etrich and K. Kern, "Plasmonic Nanowire Antennas: Experiment, Simulation, and Theory," *Nano. Lett.* vol. 10, pp. 3596-3603, 2010. doi: 10.1021/nl101921y.

[40] N.K. Grady, N.J. Halas, P. Nordlander, "Influence of dielectric function properties on the optical response of plasmon resonant metallic nanoparticles", *Chem. Phys. Lett.*, vol. 399, no. 1, pp. 167-171, 2004. https://doi.org/10.1016/j.cplett.2004.09.154.

[41] K. S. Lee and M. A. El-Sayed, "Gold and Silver Nanoparticles in Sensing and Imaging: Sensitivity of Plasmon Response to Size, Shape, and Metal Composition," *J. Phys. Chem. B.*, vol. 110, no. 39, pp. 19220-19225, 2006. doi: 10.1021/jp062536y.

[42] G. Schider et al., "Plasmon dispersion relation of Au and Ag nanowires", Phys. Rev. B, vol. 68, p. 155427, 2003.

[43] V. Amendola, R. Pilot, M. Frasconi, O. M Maragò, M. A. Iatì, "Surface plasmon resonance in gold nanoparticles: a review", *J. Phys.: Condens. Matter*, vol. 29, pp. 203002, 2017. Doi: 10.1088/1361-648X/aa60f3

[44] V. Giannini, A. I. Fernandez-Domínguez, S. C. Heck, and S. A. Maier, "Plasmonic Nanoantennas: Fundamentals and Their Use in Controlling the Radiative Properties of Nanoemitters," *Chem. Rev.*, vol. 111, pp. 3888-3912, 2011. doi: 10.1021/cr1002672

[45] A. Derkachova, K. Kolwas, and I. Demchenko, "Dielectric Function for Gold in Plasmonics Applications: Size Dependence of Plasmon Resonance Frequencies and Damping Rates for Nanospheres,"

Plasmonics. Springer, vol. 11, pp. 941-951, 2016. Doi: 10.1007/s11468-015-0128-7.

[46] S. Link, Z. L. Wang, and M. A. El-Sayed, "Alloy Formation of Gold−Silver Nanoparticles and the Dependence of the Plasmon Absorption on Their Composition", *J. Chem. Phys.*, B, vol. 103 no. 18, pp. 3529-3533, 1999. DOI: 10.1021/jp990387w

Sumitra Dey (S'14) received the B.Tech degree in Radio Physics and Electronics form University of Calcutta, Kolkata, India, in 2014 and the M.Tech. degree in RF and Microwave Communication Engineering from IIEST Shibpur, West Bengal, India, in 2016. She is currently pursuing the Ph.D. in Electrical Engineering from University of Missouri-Kansas City, USA. Her current research interests include nano-electromagnetics, nondestructive evaluation, experimental microwave and terahertz imaging, application of deep learning in antenna optimization, composite modelling using multilayer Green's functions, characteristic mode theory and applications.

She was the recipient of the Honorable Mention Award in Student paper competition in 2019 IEEE APS/USNC URSI Symposium, Atlanta, Georgia, USA, Honorable Mention Award in 2018 Altair FEKO Student Design Competition, and the Best Student Paper Award in IEEE CALCON 2015, Kolkata, India. She was awarded the GATE Scholarship (2014), Inspire Scholarship (2008) and National Merit Scholarship (2006) from the Ministry of Human Resource Development, Govt. of India. She has volunteered actively in different IEEE Student Branch Chapters in India and in USA.

Deb Chatterjee (M'99–SM'16) received the B.Tech. degree in electrical engineering from Jadavpur University, Kolkata, India, in 1982, the M.Tech. degree from IIT Kharagpur, Kharagpur, India, in 1984, the M.A.Sc. degree from Concordia University, Montréal, QC, Canada, in 1992, and the Ph.D. degree from the University of Kansas, Lawrence, KS, USA, in 1998.

He was an ONR-ASEE Summer Faculty Fellow with the Naval Research Laboratory, Washington, DC, USA, from 2009 to 2014. He is currently an Associate Professor with the Department of Computer Science and Electrical Engineering, University of Missouri at Kansas City, Kansas City, MO, USA. His current research interests include asymptotic techniques, multilayer Green's functions, characteristic mode theory and applications, electronic packaging, and microwave imaging.

Edward J. Garboczi received the B.S. degree in Physics (Highest Honors) from Michigan State University, East Lansing, Michigan, in 1980 and a Ph.D. in Condensed Matter Physics (Theory) from Michigan State University, East Lansing, Michigan, in 1985.

From 1985-1988, he was a Research Physicist in Armstrong World Industries, Inc. in Lancaster, Pennsylvania. From 1988-2014, he was a Physicist, Group Leader, and finally a Fellow at the National Institute of Standards and Technology (NIST), Materials and Structural Systems Division, Gaithersburg, Maryland. In 2014, he moved to the NIST Boulder, Colorado site in the Division of Applied Chemicals and Materials Division. His research interests include computational materials science, porous materials, electrical properties of nanocomposites, and 3D particle shape analysis of a wide range of particles including gravel, sand, cement, chemical explosives, lunar soil, and metal powder for additive manufacturing.

Dr. Garboczi is a Fellow of the American Concrete Institute (ACI), the American Ceramic Society (ACerS), and is the recipient of the ACI Robert E. Philleo award, the ACerS Della Roy Lecture Award, the ACers Edward C. Henry Best Paper Award (Electronics Division), and a Silver Medal from the Department of Commerce for the creation of the Virtual Cement and Concrete Testing Laboratory.

Ahmed M. Hassan (S'07–M'12–SM'19) received the B.Sc. degree (with highest honors) and M.Sc. degree from Cairo University, Giza, Egypt, in 2004 and 2006, respectively, both in electronics and communications engineering. He received the Ph.D. degree in electrical engineering from the University of Arkansas, Fayetteville AR, USA, in 2010.

From 2011 to 2012, he was a Postdoctoral Researcher in the Department of Electrical Engineering at the University of Arkansas. From 2012 to 2015, he was a Postdoctoral Researcher at the National Institute of Standards and Technology, Gaithersburg, MD, USA. Currently, he is an Assistant Professor at the Computer Science Electrical Engineering Department at the University of Missouri-Kansas City. His current research interests include nano-electromagnetics, bio-electromagnetics, electromagnetic compatibility and interference, nondestructive evaluation, experimental microwave and terahertz imaging.

Dr. Hassan was the recipient of the 2018 University of Missouri-Kansas City Chancellor's Early Career Award for Excellence in Teaching, the 2014 Outstanding Poster Award in the 21st Annual NIST Sigma Xi Postdoctoral Poster Presentation, and the 2007 Doctoral Academy Fellowship at the University of Arkansas.